Available online at www.sciencedirect.com
SCIENCE DIRECT®
PERGAMON
International Journal of Heat and Mass Transfer 46 (2003) 2313–2327
International Journal of HEAT and MASS TRANSFER
www.elsevier.com/locate/ijhmt

Thermosolutal transport and macrosegregation during freeze coating of a binary substance on a continuous moving object

C. Tangthieng, F.B. Cheung *

Department of Mechanical and Nuclear Engineering, The Pennsylvania State University, University Park, PA 16802, USA

Received 27 August 2002; received in revised form 6 December 2002

Abstract

The process of freeze coating of a binary substance on a continuous moving plate is investigated theoretically. A comprehensive model describing the momentum, heat, and mass transport in the freeze-coating system has been developed that accounts for the coupling between the macroscopic and microscopic aspects of the process. The problem is formulated using the single-domain approach and the governing equations are solved by the finite difference method. Effects of various controlling parameters on the freeze-coat thickness and the macrosegregation pattern have been determined. It is found that macrosegregation could be important in the freeze-coating process. As the distance from the surface of the plate is increased, the solid species concentration considerably decreases, reaching a minimum value and rising toward the ambient concentration. The macrosegregation pattern appears to be most sensitive to the equilibrium partition ratio. As the latter is increased, the difference between the solid and liquid species concentrations tends to decrease, leading to a substantial reduction of macrosegregation within the freeze coat.

Keywords: Freeze coating; Thermosolutal transport; Macrosegregation

1. Introduction

In the past two decades or so, the process of freeze coating of a molten substance on a continuously moving object have been studied quite extensively by a number of researchers [1–11]. When the coating material is made of a pure substance [1–6], the interface between the liquid and solid phases can be assumed sharp and isothermal. On the other hand, when the coating material is a binary substance [7–11], a two-phase mushy region would develop in the freeze-coating system. In addition to the moving boundaries, the coupling between the macroscopic and microscopic features of the process in the mushy region renders the problem rather complicated and difficult to solve.

Stevens and Poulikakos [7] studied the process of freeze coating in which convection in the two-phase mushy region is assumed negligible. Zhang et al. [8] utilized a continuum model developed by Bennon and Incropera [9] to analyze the hot-dip coating process where a metal rod was pulled vertically through a molten bath. The effect of the bath geometry was taken into account. Tangthieng et al. [10] studied the freeze-coating process where the plate is assumed semi-infinite in thickness. The two-phase mushy region is treated as an artificial fluid with a high viscosity. Later, Tangthieng et al. [11] extended their work by relaxing the semi-infinite plate assumption to investigate the growth-and-decay behavior of the freeze coat on a moving plate having a finite thickness. Effects of various controlling parameters of the system on the maximum freeze-coat thickness and the corresponding axial location were determined. In all of the above studies, however, the concentration field was assumed uniform throughout the system. The solute transport was not considered. Moreover,

* Corresponding author.
E-mail address: fxc4@psu.edu (F.B. Cheung).

0017-9310/03/$ - see front matter
doi:10.1016/S0017-9310(02)00538-0

Nomenclature

a^*	solid fraction ratio
A_d	effective interfacial area between equiaxed grains and interdendritic liquid
c_{drag}	unified drag term of the momentum equation ($1/m^2$)
c_p	specific heat (J/(kg-K))
C	species concentration
C_D	drag coefficient
C_{PO}	dendritic porosity correction factor
C_{SH}	non-spherical dendrites correction factor
d	a half of plate's thickness (m)
d_e	envelope volume-equivalent dendrite diameter (m)
$d_{e,p}$	envelope volume-equivalent dendrite diameter at the packing limit (m)
D_ℓ	mass diffusivity coefficient (m^2/s)
ΔH_m	latent heat of fusion (J/kg)
k	thermal conductivity (W/(m-K))
K	permeability of the dendritic structure (m^2)
K_p	permeability at the packing limit (m^2)
Le	Lewis number, Eq. (35)
m_1	slope of the solidus line (K)
m_2	slope of the liquidus line (K)
M_{drag}	drag force per unit volume (N/m^3)
n	grain density or number of particles per unit volume ($1/m^3$)
Pr	Prandtl number
R_{cap}	freeze-coat-to-wall heat capacity ratio
R_{dep}	departed-diameter-to-plate-thickness ratio
R_k	freeze-coat-to-wall thermal conductivity ratio
R_{sub}	wall subcooling parameter
R_{sup}	liquid superheating parameter
R_λ	dendrite-spacing-to-plate-thickness ratio
Re_{de}	Reynolds number based on the envelope volume-equivalent diameter
Ste	Stefan number
T	temperature (K)
T_o	inlet plate temperature (K)
T_1	solidus temperature (K)
T_2	liquidus temperature (K)
T_{max}	melting temperature of pure species A (K)
U	axial velocity (m/s)
U	dimensionless axial velocity
U_o	plate velocity (m/s)
v	vertical velocity (m/s)
V	dimensionless vertical velocity
x	Cartesian coordinate in axial direction (m)
y	Cartesian coordinate in vertical direction (m)

Greek symbols

α	thermal diffusivity (m^2/s)
β_e	normalized radius based on d_e
γ	interfacial mass transfer rate due to phase change ($kg/(s\text{-}m^3)$)
δ_1	thickness of freeze coat or vertical distance corresponding to the solidus isotherm (m)
δ_2	vertical distance corresponding to the liquidus isotherm (m)
Δ_1	dimensionless thickness of freeze coat or vertical dimensionless distance corresponding to the solidus isotherm
Δ_2	vertical dimensionless distance corresponding to the liquidus isotherm
Δ_p	vertical dimensionless distance corresponding to the packing limit isotherm
ε_ℓ	liquid volume fraction
ε_s	solid volume fraction
$\varepsilon_{s,p}$	packing limit fraction
η	dimensionless coordinate in vertical direction
κ	equilibrium partition ratio
λ_1	primary arm spacing (m)
λ_2	secondary arm spacing (m)
μ_ℓ	dynamics viscosity (kg/(m-s))
υ_ℓ	kinematics viscosity (m^2/s)
ρ	density (kg/m^3)
θ	dimensionless temperature
Ω	stretching factor used for the separate-phase flow model
ξ	dimensionless coordinate in axial direction
ψ	dimensionless concentration
ψ_e	sphericity of the dendrite envelope

Subscripts

c	liquid phase of the coating material region
eq	at equilibrium
max	maximum value
min	minimum value
mix	mixture between the liquid and solid phases
s	solid phase of the coating material region
w	wall region
∞	at ambient condition

macrosegregation in the freeze-coat layer was not seriously studied. Also the coupling between the macroscopic and microscopic aspects of the process was ignored.

In recent years, many mathematical models have been developed to predict macrosegregation during solidification process by considering the solute transport [9,12–14]. The single-domain approach, which facilitates

the numerical algorithm by eliminating the complexity of tracking nodes located at the moving interfaces, has been successfully applied to the transport equations. More sophisticated models have also been developed that take into account the microscopic features [15–22].

Most of the single-domain models [12–22], however, are restricted to solidification under the influence of natural convection. Very little studies of macrosegregation have been performed under forced-convective conditions. The only relevant works are by Kuznetsov [23,24]. In Ref. [23], a strip casting process was studied in which the alloy melt flowed and solidified over a chilled plate. A full set of momentum, energy, and solute transport equations were employed to describe the flow field, heat transfer, and macrosegregation in the system. Later, Kuznetsov [24] extended his work by examining the effects of the change of the cooling rates and the casting speeds on the macrosegregation pattern in the solidified strip.

In the present study, the process of freeze coating of a binary substance on a continuous moving plate is investigated using the single-domain approach. A comprehensive model that properly accounts for the momentum, heat, and species transport in the freeze-coating system, is developed from first principles. Supplementary models, associated with the microscopic aspects, are also incorporated into the macroscopic equations. The system of equations governing the freeze-coating process is numerically solved by employing the fully implicit finite difference method. The variations of the freeze-coat thickness and the macrosegregation pattern in the freeze coat are determined as functions of various controlling parameters of the system.

2. Problem formulation

A graphical representation of the freeze-coating system under consideration is depicted in Fig. 1. A chilled plate having a finite thickness of $2d$ at a uniform temperature T_o is continuously fed at a constant speed U_o through a liquid bath filled with a binary alloy melt. The ambient liquid temperature and concentration have constant values of T_∞ and C_∞, respectively. Because the local composition can deviate from C_∞, the local solidus and liquidus temperatures (i.e., T_1 and T_2, respectively) also differ from the solidus and liquidus temperature evaluated at C_∞ (i.e., $T_{1\infty}$ and $T_{2\infty}$, respectively). When T_o is lower than T_1, a thin solidified layer, namely a freeze coat, would form on the surface of the plate. The freeze-coat thickness δ_1 and the liquidus point δ_2 correspond to the isothermal contours of T_1 and T_2, respectively.

The region located between δ_1 and δ_2 is the two-phase mushy region. In this study, the two-phase mushy region is divided into two regions based on the dendritic configuration as shown in Fig. 2. When the solid fraction is higher than a certain limit, namely the packing limit fraction $\varepsilon_{s,p}$, the solid phase is packed together and acts as if it were a porous medium, with the interdendritic liquid flowing through it. This region is referred to as the two-phase packing region where the solid structure grows from the solidus interface in the form of columns, namely, columnar dendrites. In the freeze-coating system, because heat is extracted from the warm melt to the chilled plate, the dendrites will grow in the direction opposite to that of heat transfer, which is perpendicular to the main flow.

On the other hand, if the solid fraction is less than the packing limit fraction, the dendrites begin to break away and disperse into the surrounding liquid. Note that in a forced convection system, the main flow may cause the dendrites to break off [25]. These broken particles, namely the equiaxed dendrites, may grow independently in the radical direction through the surrounding undercooled liquid. This region is referred to as the two-phase dispersed region.

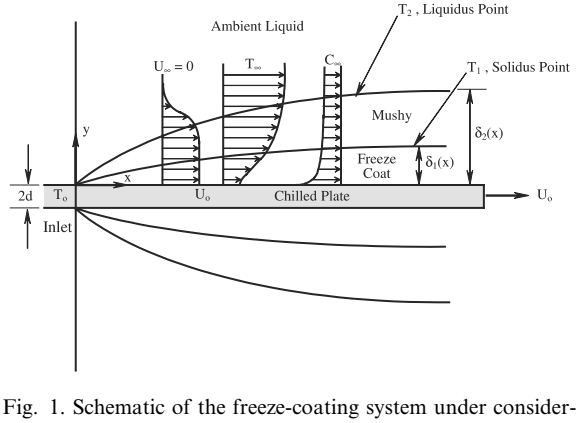

Fig. 1. Schematic of the freeze-coating system under consideration.

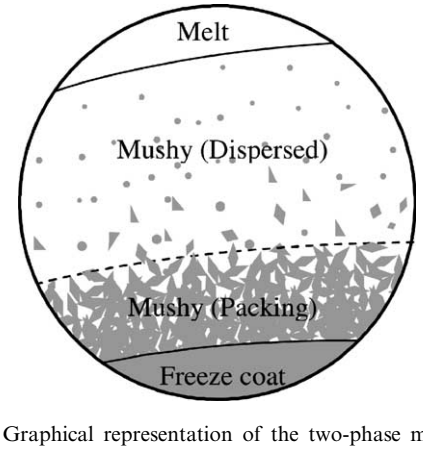

Fig. 2. Graphical representation of the two-phase mushy region consisting of the packing and dispersed regions.

The equations governing the freeze-coating system can be derived by applying the volume average theorem over a representative elemental volume or REV [13]. By utilizing the single-domain concept, the transport equations are valid throughout the entire coating material region, which physically consists of the freeze coat, the two-phase mushy, and the binary melt regions. Transition between the single-phase and the two-phase regions is implicitly resolved by the representation of variables as a function of the solid fraction. On the other hand, the moving plate is treated as a separate region, namely the wall region. To formulate the governing equations, the following assumptions are made:

(i) The system is steady and two-dimensional.
(ii) The flow is laminar. It should be noted that transition to turbulence may cause a sudden reduction of the freeze-coat thickness, which is not desirable as it has a severe negative impact on the final product [26].
(iii) The boundary layer approximation is valid. As a result, the governing equations are parabolic.
(iv) The physical properties of each phase are constant. To minimize the number of parameters, the density, the thermal conductivity, and the specific heat of both phases are assumed identical.
(v) The liquid phase in the mushy region behaves like a Newtonian fluid.
(vi) The velocity of the solid phase in the two-phase mushy region, u_s, can be expressed by the following asymptotic model:

$$u_s = (1-a^*)u_c + a^* U_o \tag{1}$$

$$v_s = (1-a^*)v_c \tag{2}$$

where

$$a^* = \min\left(1, \frac{\varepsilon_s}{\varepsilon_{s,p}}\right) = \begin{cases} 1 & \text{if } \varepsilon_s \geqslant \varepsilon_{s,p} \\ \dfrac{\varepsilon_s}{\varepsilon_{s,p}} & \text{if } \varepsilon_s < \varepsilon_{s,p} \end{cases} \tag{3}$$

These equations are referred to as the consolidation factor [27]. It can be seen that u_s is assured to behave correctly under two asymptotic cases: if ε_s is higher than $\varepsilon_{s,p}$, u_s is equal to the plate velocity, corresponding to the velocity of the columnar structure attached to the freeze coat. If ε_s approaches zero, u_s and u_c are identical. For an intermediate range of ε_s, i.e., $0 < \varepsilon_s < \varepsilon_{s,p}$, u_s is assumed linearly proportional to u_c based on the value of the local solid fraction.
(vii) Local thermal equilibrium exists for both the solid and liquid phases within the REV.
(viii) The effect of microsegregation, i.e., the variations of the solid and liquid species concentrations within the REV, is negligible. The solid and liquid species concentrations are linearly related by

$$C_s = \kappa C_c \tag{4}$$

where κ is equilibrium partition ratio.
(ix) There is no diffusion in the solid phase. The species diffusivity for the solid phase is approximately a thousand times smaller than that of the liquid phase.
(x) The dispersive flux terms, originated from the volume average procedure, are assumed negligible.

2.1. Governing equations

With the aforementioned assumptions, the governing equations and associated boundary conditions of the freeze-coating system can be written as follows:

(i) Wall region ($x \geqslant 0$ and $-d \leqslant y \leqslant 0$)

$$\rho_w c_{pw} U_o \frac{\partial T_w}{\partial x} = k_w \frac{\partial^2 T_w}{\partial y^2} \tag{5}$$

$$x = 0 : T_w = T_o \tag{6a}$$

$$y = 0 : T_w = T_c \quad \text{and} \quad k_w \frac{\partial T_w}{\partial y} = k_c \frac{\partial T_c}{\partial y} \tag{6b}$$

$$y = -d : k_w \frac{\partial T_w}{\partial y} = 0 \tag{6c}$$

(ii) Coating material region ($x \geqslant 0$ and $0 \leqslant y \leqslant \infty$)

$$\frac{\partial}{\partial x}[(1-\varepsilon_s a^*)u_c + \varepsilon_s a^* U_o] + \frac{\partial}{\partial y}[(1-\varepsilon_s a^*)v_c] = 0 \tag{7}$$

$$\begin{aligned}(1-\varepsilon_s)\rho_c u_c \frac{\partial u_c}{\partial x} &+ (1-\varepsilon_s)\rho_c v_c \frac{\partial u_c}{\partial y} \\ &= \mu_\ell (1-\varepsilon_s)\frac{\partial^2 u_c}{\partial y^2} + \mu_\ell (1-a^*)\frac{\partial \varepsilon_s}{\partial y}\frac{\partial u_c}{\partial y} \\ &\quad + \mu_\ell (U_o - u_c)\frac{\partial a^*}{\partial y}\frac{\partial \varepsilon_s}{\partial y} + \mu_\ell a^* (U_o - u_c)\frac{\partial^2 \varepsilon_s}{\partial y^2} \\ &\quad + a^*(U_o - u_c)\gamma + M_{drag}\end{aligned} \tag{8}$$

$$\rho_c c_{pc}[(1-\varepsilon_s a^*)u_c + \varepsilon_s a^* U_o]\frac{\partial T_c}{\partial x} + \rho_c c_{pc}[(1-\varepsilon_s a^*)v_c]\frac{\partial T_c}{\partial y} + \Delta H_m \gamma = k_c \frac{\partial^2 T_c}{\partial y^2} \tag{9}$$

$$\begin{aligned}\rho_c[(1-\varepsilon_s)u_c + \varepsilon_s(1-a^*)\kappa u_c + \varepsilon_s a^* \kappa U_o]\frac{\partial C_c}{\partial x} &+ \rho_c[(1-\varepsilon_s)v_c + \varepsilon_s(1-a^*)\kappa v_c]\frac{\partial C_c}{\partial y} + (1-\kappa)C_c\gamma \\ &= \rho_c D_\ell (1-\varepsilon_s)\frac{\partial^2 C_c}{\partial y^2} - \rho_c D_\ell \frac{\partial \varepsilon_s}{\partial y}\frac{\partial C_c}{\partial y}\end{aligned} \tag{10}$$

$$x = 0 : u_c = 0, \quad T_c = T_\infty, \quad \text{and} \quad C_c = C_\infty \tag{11a}$$

$$y = 0 : u_c = U_o, \quad v_c = 0, \quad T_c = T_w,$$

$$k_c \frac{\partial T_c}{\partial y} = k_w \frac{\partial T_w}{\partial y}, \quad \text{and} \quad C_c = C_c(0) \tag{11b}$$

$$y \to \infty : u_c = 0, \quad T_c = T_\infty, \quad \text{and} \quad C_c = C_\infty \tag{11c}$$

A detailed derivation of the above equations can be found in Ref. [28]. Eq. (5) is the heat conduction equation for the wall region. Eqs. (7), (9) and (10) represent the mixture form of the continuity, energy, and species equations for the coating material region whereas Eq. (8) is the momentum equation for the liquid phase alone. The velocity of the solid phase in the two-phase dispersed region is given by Eqs. (1) and (2) according to assumption (vi) whereas in the freeze coat and the two-phase packing regions, the solid velocity is the same as the moving plate velocity. In general, the mixture equations can be derived by adding the governing equations for the liquid and solid phases together. A major advantage of the mixture equations is the absence of the interfacial transfer terms, which leads to a less complicate form of the equations themselves. However, should the microscopic aspects be included, these interfacial transfer terms must appear in the governing equations because they play a key role to link the microscopic quantities to the macroscopic equations.

The term γ, appearing in Eqs. (8)–(10), is the interfacial mass transfer due to phase change, which is given by

$$\begin{aligned}\gamma &= \frac{\partial}{\partial x}(\varepsilon_\ell \rho_c u_c) + \frac{\partial}{\partial y}(\varepsilon_\ell \rho_c v_c) \\ &= \frac{\partial}{\partial x}[(1-\varepsilon_s)\rho_c u_c] + \frac{\partial}{\partial y}[(1-\varepsilon_s)\rho_c v_c]\end{aligned} \tag{12}$$

Physically, γ represents the amount of liquid phase within the REV, which transforms to the solid phase. The value of γ is negative during the freezing process because the amount of liquid phase within the REV decreases. In contrast, it is positive when remelting occurs and zero for the pure liquid and pure solid regions in which phase change does not take place. In the momentum equation, the fifth term on the right-hand side of Eq. (8) is a combination of the interfacial momentum transfer due to phase change and the inertia terms, which can be written in terms of γ. In the energy and species equations (Eqs. (9) and (10)), the terms containing γ, are the energy source term (i.e., the latent heat effect) and the species source term, respectively.

The second and third terms on the right-hand side of Eq. (8) are the terms originated from the consolidation factor (Eqs. (1) and (2)), which only appears in the two-phase dispersed region. The fourth term on the right-hand side of Eq. (8) is a combination of the viscous term and the effect of the consolidation factor. The sixth term on the right-hand side of Eq. (8) is the interfacial stress transfer, which is discussed next.

2.2. Supplementary equations

The term M_{drag} appearing in the last term of the right-hand side of Eq. (8) represents the interfacial drag force (per unit volume) between the liquid and solid phases within the REV. For the two-phase packing region, M_{drag} can be modeled by analogy with the Darcy law, which have been reported by many researchers [9,19,20]. The value of M_{drag} for this region is given by [13]

$$M_{drag} = \frac{\varepsilon_\ell^2 \mu_\ell}{K}(U_o - u_c) \tag{13}$$

where K is the permeability of the packed structure. In the freeze-coating process, the direction of the main flow is perpendicular to the primary dendrite arm. Thus the permeability of the columnar dendrite under this flow arrangement is given by [29]

$$K = 1.73 \times 10^{-3}\left(\frac{\lambda_1}{\lambda_2}\right)^{1.09} \lambda_2^2 \frac{\varepsilon_\ell^3}{(1-\varepsilon_\ell)^{0.749}} \tag{14}$$

where λ_1 and λ_2 are the primary and secondary dendrite arm spacing, respectively.

For the two-phase dispersed region, M_{drag} can be modeled in analogy with the drag force from flow over an object:

$$M_{drag} = \frac{1}{2}\frac{\rho_c A_d C_D}{V_o}|u_s - u_c|(u_s - u_c) \tag{15}$$

where C_D is the drag coefficient [30,31]. Due to the irregular shape of the equiaxed grains, a concept of dendrite envelope [32], is utilized by creating a solid sphere, which has the same volume as the dendrite. Because an average size of the equiaxed particles is on the order of 10^{-4} to 10^{-5} m, the flow over a dendrite-volume-equivalent sphere will be in the Stokes regime. Hence, the drag coefficient can be written as

$$C_D = \frac{24}{Re_{de}}\frac{C_{PO}}{C_{SH}} \tag{16}$$

where Re_{de} is the Reynolds number based on the envelope volume-equivalent diameter, d_e, which can be written as

$$Re_{de} = \frac{\rho_c |u_s - u_c| d_e}{\mu_\ell} \tag{17}$$

In Eq. (16), C_{SH} and C_{PO} represent the correction factors, which account for the effects of non-spherical shape and the porosity of the dendrite, respectively. The correlation for C_{SH} is given by

$$C_{SH} = 1.2376 \log_{10}\left(\frac{\psi_e}{0.1556}\right) \tag{18}$$

where ψ_e is the envelope sphericity. For simplicity, ψ_e is assumed to be unity for the freeze-coating process. As a result, the value C_{SH} from the above equation is also equal to unity. On the other hand, the correlation for C_{PO} is given by

$$C_{PO} = \frac{2\beta_e^2\left(1 - \frac{\tanh(\beta_e)}{\beta_e}\right)}{2\beta_e^2 + 3\left(1 - \frac{\tanh(\beta_e)}{\beta_e}\right)} \tag{19}$$

where the normalized radius β_e is defined as

$$\beta_e = \frac{d_e}{2\sqrt{K_p}} \tag{20}$$

K_p is the intrinsic permeability within the dendrite envelope. Because an equiaxed dendrite is a broken part of the columnar structure, it is assumed that the value of the intrinsic permeability is constant throughout the dispersed region and is equal to the permeability of the columnar structure evaluated at the packing limit fraction, i.e., from Eq. (14)

$$K_p = 1.73 \times 10^{-3}\left(\frac{\lambda_1}{\lambda_2}\right)^{1.09}\lambda_2^2\frac{(1-\varepsilon_{s,p})^3}{\varepsilon_{s,p}^{0.749}} \tag{21}$$

The envelope volume-equivalent diameter, d_e is geometrically related to the grain density (or the number of equiaxed particles per unit volume), n, as follows:

$$d_e = \left(\frac{6}{\pi n}\frac{\varepsilon_s}{\varepsilon_{s,p}}\right)^{1/3} \tag{22}$$

In the freeze-coating process, the grain density is assumed constant and treated as a controlling parameter. By setting $\varepsilon_s = \varepsilon_{s,p}$, the above equation becomes

$$d_{e,p} = \left(\frac{6}{\pi n}\right)^{1/3} \tag{23}$$

where $d_{e,p}$ is the envelope volume-equivalent diameter at the packing limit fraction or the departed diameter. Substituting Eqs. (16), (17) and (23) into Eq. (15) and rearranging yields

$$M_{drag} = 18\mu_\ell\frac{C_{PO}}{C_{SH}}\left(\frac{1}{d_{e,p}}\right)^2\left(\frac{\varepsilon_s}{\varepsilon_{s,p}}\right)^{4/3}(U_o - u_c) \tag{24}$$

Thus, the unified drag force for both the two-phase packing and dispersed regions can be written as

$$M_{drag} = \mu_\ell c_{drag}(U_o - u_c) \tag{25}$$

where

$$c_{drag} = \begin{cases} \dfrac{\varepsilon_s^{0.749}}{1.73\times10^{-3}(\lambda_1/\lambda_2)^{1.09}\lambda_2^2(1-\varepsilon_s)} & \text{if } \varepsilon_s \geqslant \varepsilon_{s,p} \\ 18\dfrac{C_{PO}}{C_{SH}}\left(\dfrac{1}{d_{e,p}}\right)^2\left(\dfrac{\varepsilon_s}{\varepsilon_{s,p}}\right)^{4/3} & \text{if } \varepsilon_s < \varepsilon_{s,p} \end{cases} \tag{26}$$

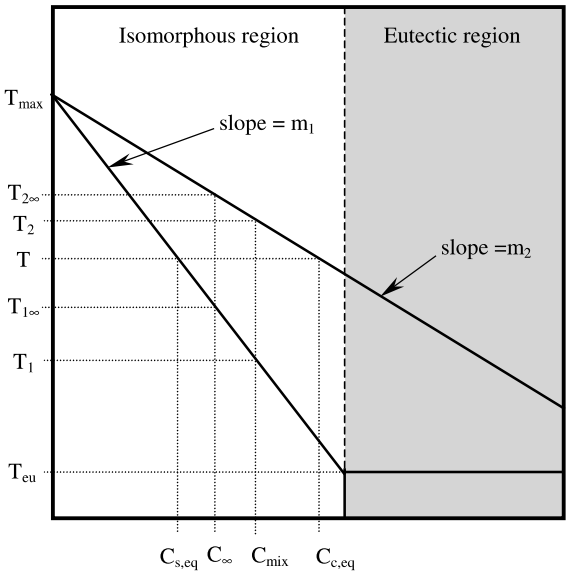

Fig. 3. Simplified equilibrium phase diagram.

2.3. Coupling of the thermal and concentration fields

Only an isomorphous alloy will be considered in this study as shown in Fig. 3. In the isomorphous region as represented by the white area of the figure, both constituents of the binary alloy are completely soluble in the solid and liquid phases without forming of a eutectic structure. In addition, the solidus and liquidus lines are assumed straight lines. It follows that the equilibrium partition ratio, κ, defined as $\kappa = m_2/m_1$, is also a constant, and the equilibrium solid and liquid species concentrations (i.e., $C_{s,eq}$ and $C_{c,eq}$, respectively) are linear functions of temperature:

$$C_{s,eq} = \frac{T - T_{max}}{m_1} \quad \text{and} \quad C_{c,eq} = \frac{T - T_{max}}{m_2} = \frac{T - T_{max}}{\kappa m_1} \tag{27}$$

It should be noted that the liquid species concentration, C_c calculated from the species equation represent the non-equilibrium liquid species concentration as a result of the solute transport. The mixture concentration is then shifted from its initial value, leading to macrosegregation during solidification. In the freeze-coating system, the thermal–solutal process is assumed quasi-equilibrium. Thus, the value of the shifted mixture concentration can be expressed by

$$C_{mix} = \varepsilon_{s,eq}C_s + \varepsilon_{\ell,eq}C_c = \varepsilon_{s,eq}C_s + (1 - \varepsilon_{s,eq})C_c \tag{28}$$

where $\varepsilon_{s,eq}$ is the solid fraction calculated from the equilibrium state, which is given by

$$\varepsilon_{s,eq} = \frac{T_{2\infty} - T}{(T_{2\infty} - T) + \kappa(T - T_{1\infty})} \tag{29}$$

The above expression implies that the equilibrium solid fraction, $\varepsilon_{s,eq}$ is only a function of temperature because the equilibrium species concentration can be written as a function of temperature (Eq. (27)). Substituting Eq. (4) into Eq. (28) yields

$$C_{mix} = [1 - (1 - \kappa)\varepsilon_{s,eq}]C_c \tag{30}$$

Once the value of the shifted mixture concentration has been determined, the solid fraction can be updated by [28]

$$\varepsilon_s = \frac{1}{1-\kappa} - \frac{\kappa}{(1-\kappa)^2}\frac{C_{mix}}{C_\infty}\frac{T_{2\infty} - T_{1\infty}}{T_{max} - T} \tag{31}$$

3. Numerical analysis

The governing equations and associated boundary conditions can be transformed to a set of dimensionless governing equations by introducing new coordinates and new dependent variables as follows:

(i) Wall region

$$\xi = \frac{x\alpha_c}{U_o d^2}, \quad \eta_w = \frac{y}{d}, \quad \text{and} \quad \theta_w = \frac{T_w - T_o}{T_\infty - T_o} \tag{32}$$

where $\xi > 0$, $-1 \leqslant \eta_w \leqslant 0$, and $0 \leqslant \theta_w \leqslant \theta_w(0)$.

(ii) Coating material region

$$\xi = \frac{x\alpha_c}{U_o d^2}, \quad \eta_c = 1 - \exp\left(-\frac{\Omega y}{d}\right)$$

$$U_c = \frac{u_c}{U_o}, \quad V_c = \frac{v_c d}{\alpha_c},$$

$$\theta_c = \frac{T_c - T_o}{T_\infty - T_o}, \quad \text{and} \quad \psi_c = \frac{C_c}{C_\infty} \tag{33}$$

where $\xi > 0$, $0 \leqslant \eta_c \leqslant 1$, $0 \leqslant U_c \leqslant 1$, $V_c \geqslant 0$, $\theta_c(0) \leqslant \theta_c \leqslant 1$, and $\psi_c \geqslant 0$.

A stretching factor, Ω is introduced in an exponential fashion to transform a semi-infinite domain in the original physical system to a finite domain. The stretching factor could be a function of ξ. Consequently, the grid can be either clustered near the wall or stretched to the far field as the algorithm marches downstream.

Due to space limitation, the dimensionless governing equations, which can be found in [28], are not presented here. Inspection of the governing system indicates that there are two microscopic and nine macroscopic parameters controlling the freeze-coating process. The two microscopic controlling parameters are the dendrite-spacing-to-plate-thickness ratio and the departed-diameter-to-plate-thickness ratio defined as

$$R_\lambda = \frac{\lambda_2}{d} \quad \text{and} \quad R_{dep} = \frac{d_{e,p}}{d} \tag{34}$$

The nine macroscopic parameters controlling the freeze-coating process are

$$R_k = \frac{k_c}{k_w}, \quad R_{cap} = \frac{\rho_c c_{pc}}{\rho_w c_{pw}}, \quad R_{sub} = \frac{T_{1\infty} - T_o}{T_{2\infty} - T_{1\infty}},$$

$$R_{sup} = \frac{T_\infty - T_{2\infty}}{T_{2\infty} - T_{1\infty}}, \quad Pr = \frac{\upsilon_\ell}{\alpha_c}, \quad Le = \frac{\alpha_c}{D_\ell},$$

$$Ste = \frac{C_{pc}(T_{2\infty} - T_{1\infty})}{\Delta H_m}, \quad \kappa = \frac{m_2}{m_1}, \quad \text{and} \quad \varepsilon_{s,p} \tag{35}$$

The system of dimensionless governing equations is solved numerically by employing the finite difference method. In so doing, the momentum, energy, and species equations are first linearized, with the linearized coefficients at the upstream location being evaluated using the "lagging"-coefficient technique [33,34]. These equations are then discretized using the fully implicit scheme resulting in a system of linear algebra, which have a tridiagonal matrix of coefficients. The Thomas algorithm is employed to solve for the U-velocity, temperature and concentration fields. The linearized coefficients are updated by a simple iterative procedure, until the solution meets the convergence criteria. The prescribed tolerances are set to be 10^{-9} for the uniform vector norm of the U-velocity, temperature, and concentration solution vectors. To maximize the convergence rate, under-relaxation factors for these three vectors are set to be 0.7, 0.8, and 0.8, respectively, and it takes approximately 10 iterations for the solution vectors to converge. For the continuity equation, a superficial V-velocity defined as the product of V_c and $(1 - \varepsilon_s)$ is introduced to facilitate numerical computation. The superficial V-velocity and the interfacial mass transfer due to phase change can be explicitly determined. The numerical calculation of the superficial V-velocity and the interfacial mass transfer due to phase change starts at $\eta_c = 0$ and moves upward to the final node in the liquid region.

From the numerical experiments, it is found that the overall convergence rate strongly depends on how fast the solid fraction can converge. Although the solid fraction can be explicitly determined by the thermal–solute coupling (Eq. (31)) after the temperature and concentration fields have been solved, an under-relaxation factor must be used to ensure the convergence of the solid fraction. The prescribed tolerances for the solid fraction vector are set to be 10^{-9}. The relaxation factor used for the solid fraction is in the range of 0.05–0.1, and it takes approximately 200–300 iterations to obtain a convergent solid fraction. The cause for the retardation of the convergence rate is found to stem from the energy source term. Note that this similar problem due to the energy source term has been reported in [23]. Although a source term linearization is recommended to improve the convergence rate, in this model where the solid fraction is a function of both temperature and

concentration, the energy source term linearization yields a further complicated form for the energy equation, which is numerically unfavorable.

After the solution has converged, three dimensionless thicknesses, indicating the freeze-coat thickness Δ_1, the location corresponding to the packing limit fraction Δ_p, and the liquid point Δ_2, are determined by the linear interpolation of the locations where the solid fraction is equal to zero, the packing limit fraction, and unity, respectively. The algorithm marches along the time-like coordinate (i.e., ξ-direction) until the freeze coat reaches its maximum thickness $\Delta_{1,max}$ corresponding to the axial location ξ_{max}. The solid species concentration within the freeze-coat layer, which reveals the macrosegregation pattern, is directly determined from the species equation.

An examination of grid independence of the numerical results is performed for a given set of controlling parameters for the baseline case ($R_k = 1$, $R_{cap} = 1$, $R_{sub} = 5$, $R_{sup} = 1$, $Pr = 0.1$, $Le = 1000$, $Ste = 0.1$, $\kappa = 0.3$, $\varepsilon_{s,p} = 0.6$, $R_\lambda = 0.005$, and $R_{dep} = 0.01$), for different values of $\Delta\xi$, $\Delta\eta$, Ω, and $d\Omega/d\xi$. In determining the maximum freeze-coat thickness, it was found that for $1.5 \leqslant \Omega \leqslant 2$, $\Delta\xi$ less than 0.1% of ξ, $\Delta\eta_w$ less than 1/800, and $\Delta\eta_c$ less than 1/1600, the numerical solutions are independent of the grid structure. The relative error in the computed results (i.e., ξ_{max} and $\Delta_{1,max}$) was found to be less than 0.2%. On the other hand, in determining the macrosegregation pattern, it was found that for $20 \leqslant \Omega \leqslant 25$, $\Delta\xi$ less than 1×10^{-4}, $\Delta\eta_w$ less than 1/1600, and $\Delta\eta_c$ less than 1/3200, the numerical solutions are independent of the grid structure. The relative error of $\psi_{c,min}$ was found to be less than 0.25%. Note that by investigating the effect of the $d\Omega/d\xi$ term on the numerical accuracy, this term can create an artificial vertical flow, similar to the V-velocity effect. This V-velocity-like behavior leads to deterioration in the numerical accuracy, especially in the species equation where diffusion is overpowered by convection. Thus, it is recommended that $d\Omega/d\xi$ be set to zero. Detailed description of the numerical algorithm can be found in [28].

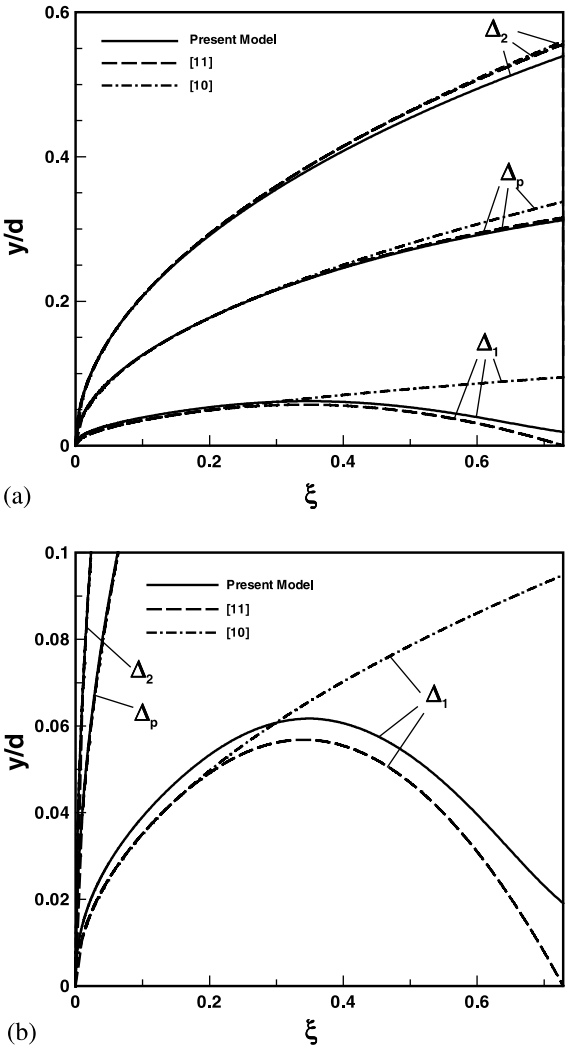

Fig. 4. Axial variations of the dimensionless coating thicknesses for the baseline case. Comparison between three different approaches: (a) for the freeze coat and the two-phase mushy regions and (b) with emphasis on the freeze coat only.

4. Results and discussion

Comparison of the axial variations of Δ_1, Δ_p, and Δ_2 predicted by the present model with those reported in [10,11] for the baseline case is depicted in Fig. 4(a) and (b). It can be seen from Fig. 4(a) that the variations of Δ_p and Δ_2 obtained from all three approaches are qualitatively the same. Also, the growth-and-decay behavior of Δ_1 predicted by the present model is similar to that predicted by Ref. [11]. This growth-and-decay behavior is due to a limited wall capacity that can be absorbed by the finite plate from the liquid. In Fig. 4(b), it can be seen that the value of Δ_1 obtained from the present model is thicker than that reported in [11]. In addition, the value of the corresponding location, ξ_{max} is also larger. A physical explanation for an increase of $\Delta_{1,max}$ is that it is caused by a flow in the transverse direction near the inlet. This vertical flow mixes the local liquid species concentration with a dilute liquid concentration from the far field. As a result, when this portion of liquid freezes, the value of the solid species concentration is lower than its values at an equilibrium state. Based on the equilibrium phase diagram, the solidus temperature is higher compared to the solidus temperature evaluated at C_∞, leading to a thicker freeze coat. The value of ξ_{max} also increases due to the fact that it would take longer time to reach a higher value of

$\Delta_{1,\max}$. Thus, the present model provides a more realistic estimate of the freeze-coat thickness than [11], as the solute transport was not modeled in [11].

The normalized solid and liquid species concentrations profile obtained by the present model are depicted in Fig. 5(a). For the freeze-coat region, despite the logarithmic scale, it can be seen that the solid species concentration is equal to the initial concentration, C_∞ at $y/d = 0$. It decreases to a minimum value, which is approximately 40% of C_∞, at $y/d = 0.0015$. Then, it increases and asymptotically approaches C_∞ until it reaches the inner edge of the two-phase mushy region at $y/d = 0.07$. The mechanism responsible for this behavior of ψ_s can be explained as follows. In the growth regime, the change of ψ_s in the freeze-coat region is caused by convection, diffusion, and the species source within a thin layer, namely the buffer layer, above the freeze coat itself. This buffer layer is a portion of the two-phase packing region where the solid fraction is nearly unity, and this portion is soon to become the freeze coat itself in the adjacent downstream location. Once this portion becomes solidified, the value of the solid species concentration remains unchanged (unless remelting occurs) as it moves downstream due to the absence of diffusion, vertical flow, and the source term in the species equation. In Fig. 5(a), ψ_s decreases due to the effect of the vertical flow within the buffer layer. In contrast, ψ_s tends to increase due to the effect of the species source term. For solidification near the inlet, the effect of the vertical flow appears to overpower that of the species source term, resulting in the lower value of ψ_s as shown in Fig. 5(a). As solidification progresses downstream, the effect of vertical flow decreases due to the higher value of the U-velocity compared to the quiescent flow near the inlet. Hence, ψ_s eventually increases as shown in Fig. 5(a). For the two-phase mushy region, the solid species concentration decreases toward the outer edge of the two-phase mushy region. On the other hand, the liquid species concentration starts at the value of approximately 3.3 at the inner edge of the two-phase mushy region, decreases with increasing y/d, and asymptotically approaches C_∞ to match the boundary condition in the liquid region. Note that in the two-phase mushy region, the relation between the solid and liquid species concentrations (Eq. (4)) holds. Therefore, the change of both concentrations must be in the same direction. Fig. 5(b) depicts comparison between variation of the mixture concentration along the vertical axis obtained from the present model and a constant mixture concentration employed in [11] where the macrosegregation is assumed negligible. It can be seen that a large deviation of the mixture concentration occurs in the freeze-coat layer near the surface of the plate. As y/d is increased, the mixture concentration asymptotically approaches the ambient concentration. The minimum value of the mixture concentration is approximately 40% of C_∞.

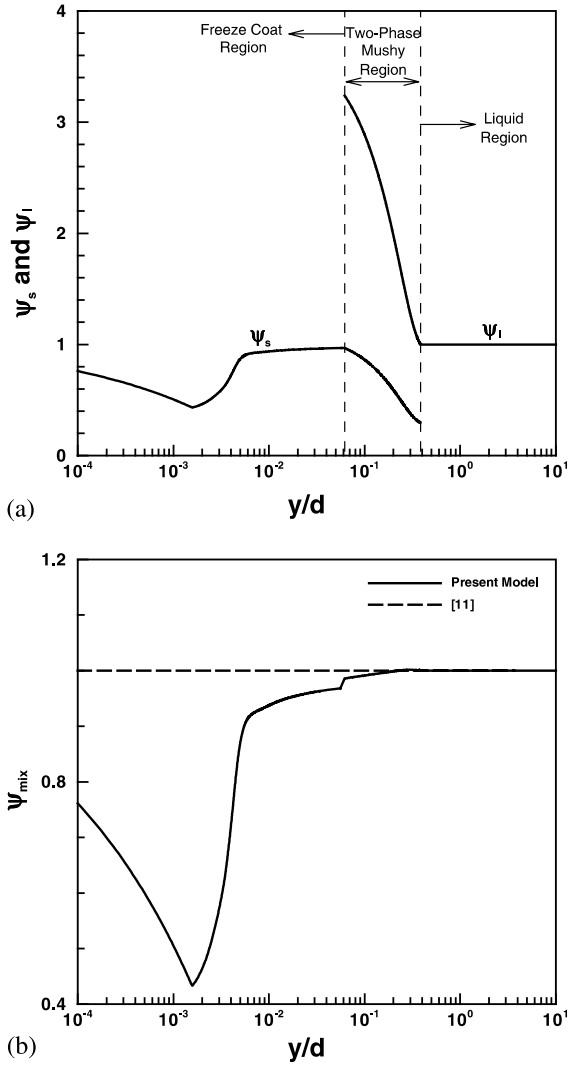

Fig. 5. (a) Normalized solid and liquid species concentration profiles at the location corresponding to the maximum freeze-coat thickness and (b) normalized mixture species concentration profiles: comparison between two different models.

The variations of $\xi_{\max}$ and $\Delta_{1,\max}$ with R_{sub} are depicted in Fig. 6(a). The values of $\xi_{\max}$ and $\Delta_{1,\max}$ obtained from the present study are larger than those obtained from the model developed in [11]. When R_{sub} is decreased to approximately four, according to the results from [11], the freeze coat would no longer form due to insufficient wall subcooling. However, at the same value of R_{sub}, a freeze coat would form according to the results predicted by the present model. As we have already discussed, a reduction of the solid species concentration due to the suction flow can lead to an increase in the solidus temperature. As a result, the freeze coat would be able to form at a higher freezing temperature.

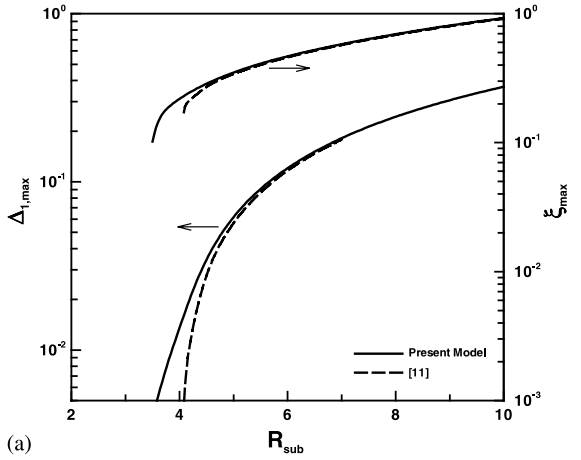

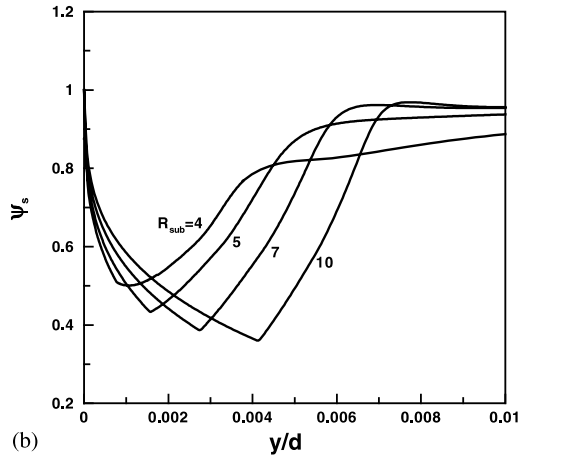

Fig. 6. Effects of the wall subcooling parameter ($R_k = 1$, $R_{cap} = 1$, $R_{sup} = 1$, $Pr = 0.1$, $Le = 1000$, $Ste = 0.1$, $\kappa = 0.3$, $\varepsilon_{s,p} = 0.6$, $R_\lambda = 0.005$, and $R_{dep} = 0.01$) on (a) the maximum freeze-coat thickness and the corresponding axial location and (b) the normalized species concentration of the freeze coat.

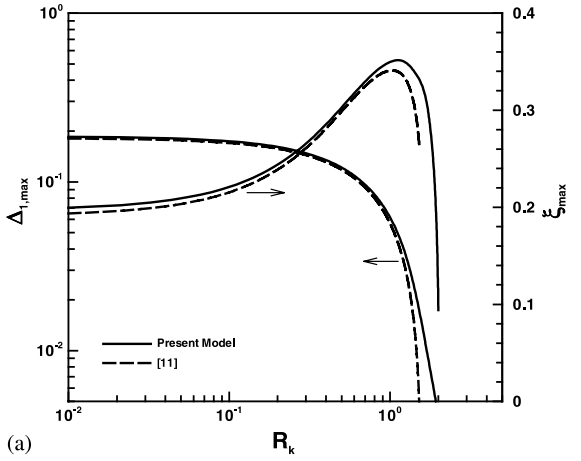

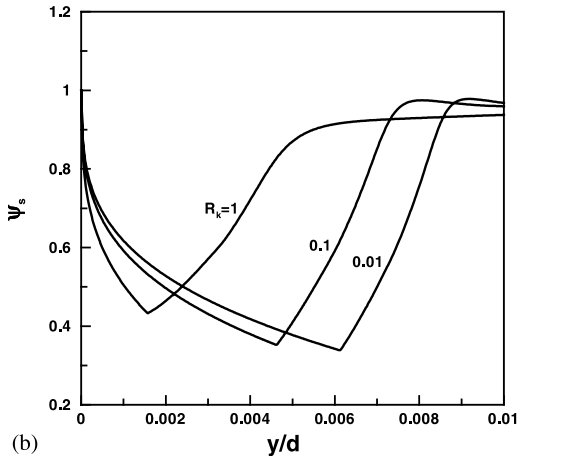

Fig. 7. Effects of the freeze-coat-to wall thermal conductivity ratio ($R_{sup} = 5$, $R_{cap} = 1$, $R_{sup} = 1$, $Pr = 0.1$, $Le = 1000$, $Ste = 0.1$, $\kappa = 0.3$, $\varepsilon_{s,p} = 0.6$, $R_\lambda = 0.005$, and $R_{dep} = 0.01$) on (a) the maximum freeze-coat thickness and the corresponding axial location and (b) the normalized species concentration of the freeze coat.

Fig. 6(b) depicts the variations of ψ_s within the freeze-coat later at different values of R_{sub}. As R_{sub} is increased, the transverse location corresponding to $\psi_{s,min}$ increases. An explanation for this is that the freeze coat is thicker with increasing R_{sub}; therefore, the effect of the species source term, which is a function γ, would take place at a higher value of y/d. In addition, because increasing R_{sub} yields a higher cooling condition, the value of γ would increase. Hence, ψ_s would increase and reach a higher plateau.

The variations of ξ_{max} and $\Delta_{1,max}$ with R_k are depicted in Fig. 7(a). It can be seen that as R_k is increased, ξ_{max} increases because it would take longer time for a low-conductive material to reach $\Delta_{1,max}$. When R_k is increased to a certain value, ξ_{max} increases and reaches the maximum value at first. Then, it begins to rapidly decrease to zero, and so does $\Delta_{1,max}$. This implies that the thermal conductivity of the wall is too low to conduct enough amount of heat to generate the freeze coat. Note that ξ_{max} and $\Delta_{1,max}$ predicted by the model developed in this study are larger than those reported in [11] with the same reason given previously. The effect of R_k on the species concentration profiles is depicted in Fig. 7(b). As R_k is decreased, $\psi_{s,min}$ is located at a higher value of y/d. Due to the fact that decreasing R_k yields a higher cooling condition, the behavior of ψ_s with decreasing R_k is qualitatively similar to that with increasing R_{sub} as shown in Fig. 6(b).

Fig. 8(a) depicts the variations of ξ_{max} and $\Delta_{1,max}$ with R_{sup}. As R_{sup} is increased, ξ_{max} and $\Delta_{1,max}$ decrease because of higher liquid superheating. By comparing ξ_{max} and $\Delta_{1,max}$ predicted by the present models and those reported in [11], the former are higher than the latter as

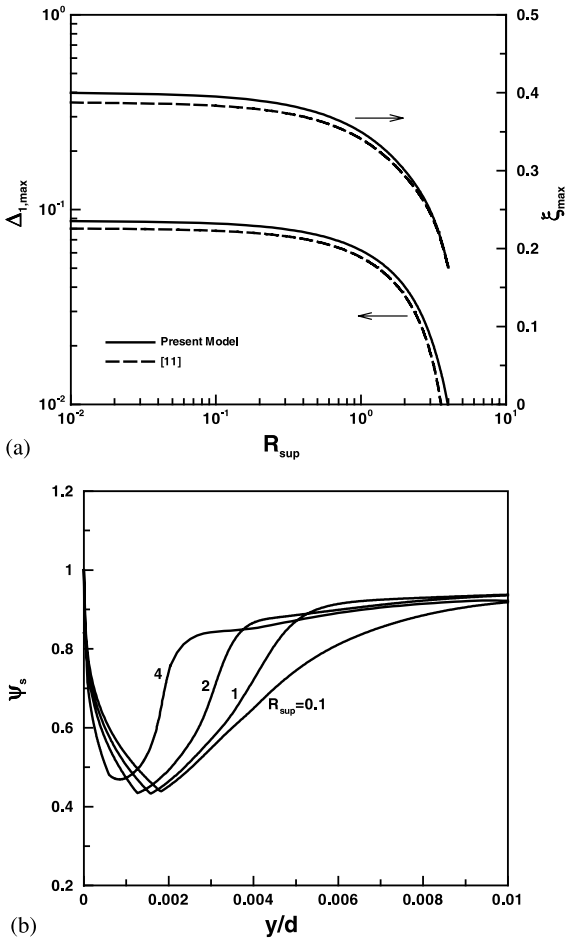

Fig. 8. Effects of the liquid superheating parameter ($R_{sub} = 5$, $R_k = 1$, $R_{cap} = 1$, $Pr = 0.1$, $Le = 1000$, $Ste = 0.1$, $\kappa = 0.3$, $\varepsilon_{s,p} = 0.6$, $R_\lambda = 0.005$, and $R_{dep} = 0.01$) on (a) the maximum freeze-coat thickness and the corresponding axial location and (b) the normalized species concentration of the freeze coat.

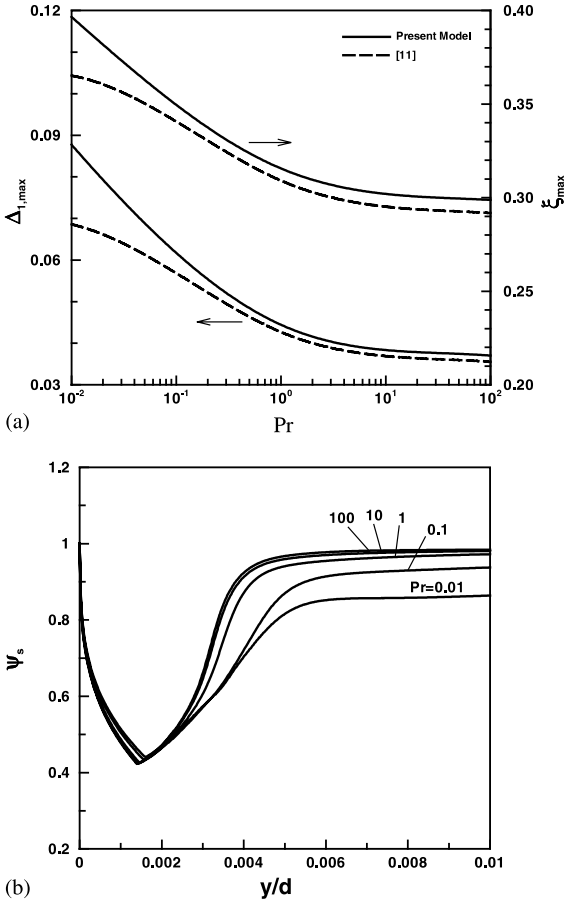

Fig. 9. Effects of the Prandtl number ($R_{sub} = 5$, $R_k = 1$, $R_{cap} = 1$, $R_{sup} = 1$, $Le = 1000$, $Ste = 0.1$, $\kappa = 0.3$, $\varepsilon_{s,p} = 0.6$, $R_\lambda = 0.005$, and $R_{dep} = 0.01$) on (a) the maximum freeze-coat thickness and the corresponding axial location and (b) the normalized species concentration of the freeze coat.

expected. However, when ξ_{max} and $\Delta_{1,max}$ get smaller, there is not much difference between the results obtained from these two models. The reason is that R_{sup} has only a secondary effect on the freeze-coat thickness compared to R_{sub}, R_k, and R_{cap}. In Fig. 8(b), the variation of ψ_s with decreasing R_{sup} is qualitatively similar to that with increasing R_{sub}. Decreasing R_{sup} leads to a better cooling condition from the plate to the warm liquid.

The variations of ξ_{max} and $\Delta_{1,max}$ with Pr are depicted in Fig. 9(a). ξ_{max} and $\Delta_{1,max}$ increase with decreasing Pr due to a lower heat transfer coefficient of the flow in the melt. It should be noted that the difference between ξ_{max} and $\Delta_{1,max}$ predicted by the present model and those reported in [11] increases as Pr gets smaller. Nonetheless, the effect of Pr on ξ_{max} and $\Delta_{1,max}$ is minor compared to that of R_{sub}, R_k, R_{cap}, and R_{sup}. The effect of Pr on ψ_s is depicted in Fig. 9(b). It can be seen that the value of $\psi_{s,min}$ is not sensitive to the change of Pr. However, when ψ_s increases beyond $\psi_{s,min}$, the value of ψ_s is lower for the case of lower Pr. The reason is that in the freeze-coat region the axial velocity is equal to U_o owing to the dominance of the Darcy term in the momentum equation, regardless of Pr. Thus, when Pr gets smaller, the momentum boundary layer becomes relatively thinner. Hence, the axial velocity begins decreasing at the inner edge of the two-phase packing region, and substantially decreases toward the edge of the momentum boundary layer. As a result, to satisfy the continuity equation, the V-velocity increases, causing the lower value of ψ_s. Note that an asymptotic behavior of the profile of ψ_s as Pr becomes sufficiently large ($Pr > 10$) is observed.

Fig. 10(a) depicts the effects of κ on ξ_{max} and $\Delta_{1,max}$. As κ is increased, ξ_{max} and $\Delta_{1,max}$ increase due to a lower value of the solid fraction in the mushy region, but the freeze coat becomes thicker. There is a slight difference

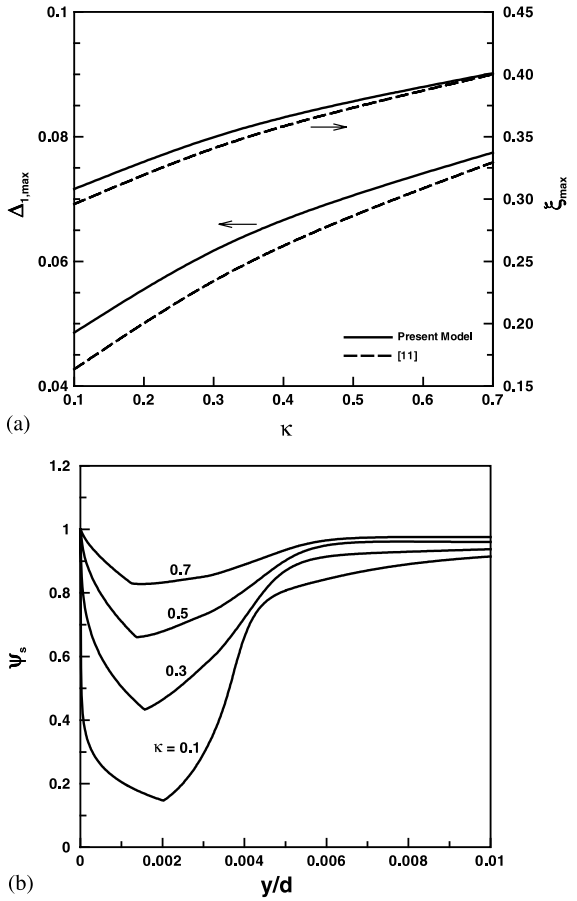

Fig. 10. Effects of the equilibrium partition ratio ($R_{sub} = 5$, $R_k = 1$, $R_{cap} = 1$, $R_{sup} = 1$, $Pr = 0.1$, $Le = 1000$, $Ste = 0.1$, $\varepsilon_{s,p} = 0.6$, $R_\lambda = 0.005$, and $R_{dep} = 0.01$) on (a) the maximum freeze-coat thickness and the corresponding axial location and (b) the normalized species concentration of the freeze coat.

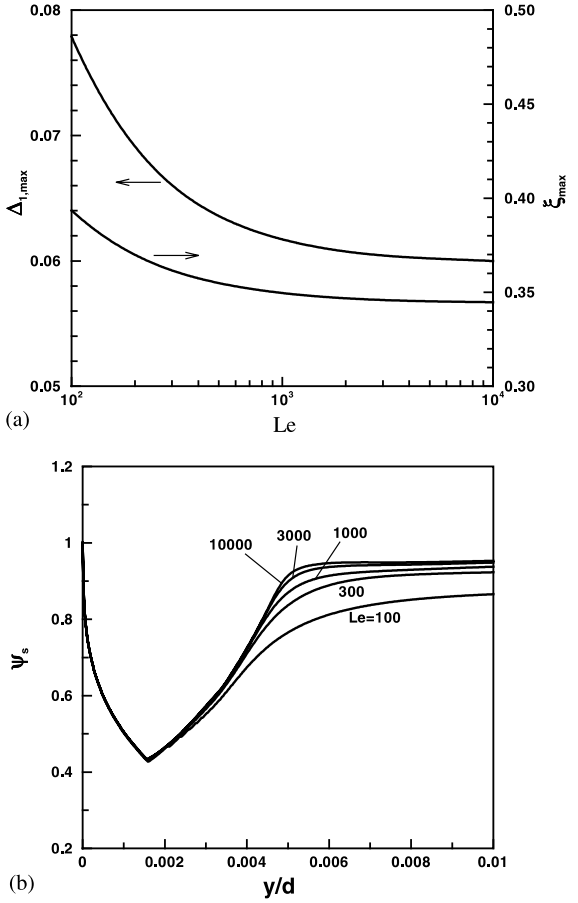

Fig. 11. Effects of the Lewis number ($R_{sub} = 5$, $R_k = 1$, $R_{cap} = 1$, $R_{sup} = 1$, $Pr = 0.1$, $Ste = 0.1$, $\kappa = 0.3$, $\varepsilon_{s,p} = 0.6$, $R_\lambda = 0.005$, and $R_{dep} = 0.01$) on (a) the maximum freeze-coat thickness and the corresponding axial location and (b) the normalized species concentration of the freeze coat.

between ξ_{max} and $\Delta_{1,max}$ obtained from the present model and those reported in [11], with higher values for the latter. The effect of κ on ψ_s is depicted in Fig. 10(b). Interestingly, macrosegregation within the freeze-coat layer substantially decreases with increasing κ. The value of $\psi_{s,min}$ also decreases from 0.15 to 0.82 as κ is increased from 0.1 to 0.7. An explanation for this is that from Eq. (4), the ratio of the solid-to-liquid species concentrations within the REV is equal to κ. As the value of approaches unity, the difference between the solid and liquid species concentrations becomes smaller, leading to a smaller variation of ψ_s during solidification.

The variations of ξ_{max} and $\Delta_{1,max}$ with Le obtained by the present model are depicted in Fig. 11(a). It can be seen that as Le is decreased, ξ_{max} and $\Delta_{1,max}$ marginally increases. Hence, the effect of Le on ξ_{max} and $\Delta_{1,max}$ is considered minor. A physical explanation for this can be seen from Figs. 9(a)–11(a), as ξ_{max} and $\Delta_{1,max}$ are more sensitive to the change of Pr than that of Le. The effect of Le on ψ_s is depicted in Fig. 11(b). There is virtually no different at the early stage of solidification when ψ_s decreases to $\psi_{s,min}$. However, beyond $\psi_{s,min}, \psi_s$ increases and asymptotically approaches to unity at a faster rate with increasing Le because the concentration boundary layer is thinner. In addition, as Le is smaller, the deviation from the asymptotic value of ψ_s becomes larger, leading to a higher value of the solidus temperature. Consequently, the values of ξ_{max} and $\Delta_{1,max}$ would be larger as shown in Fig. 11(a). Note that $\xi_{max}, \Delta_{1,max}$, and the profile of ψ_s appear to approach an asymptotic behavior as Le is sufficiently large ($Le > 3000$).

The effect of R_λ on $\xi_{max}, \Delta_{1,max}$ and ψ_s is presented in Table 1. It is clear that $\xi_{max}, \Delta_{1,max}$, and ψ_s are insensitive to the change of R_λ. As R_λ is increased from 0.001 to 0.01, ξ_{max} and $\Delta_{1,max}$ increase only by 0.06% and 0.2%, respectively.

Table 1
Effects of the dendrite-spacing-to-plate-thickness ratio ($R_{sub} = 5$, $R_k = 1$, $R_{cap} = 1$, $R_{sup} = 1$, $Pr = 0.1$, $Le = 1000$, $Ste = 0.1$, $\kappa = 0.3$, $\varepsilon_{s,p} = 0.6$, and $R_{dep} = 0.01$) on the maximum freeze coat thickness and the corresponding axial location

R_λ	$\xi^{(1)}_{max}$	$\Delta^{(1)}_{1,max}$
0.001	0.349458	0.0616566
0.002	0.349505	0.0616714
0.005	0.349634	0.0617153
0.01	0.349672	0.0617850

Fig. 12(a) depicts the effect of R_{dep} on ξ_{max} and $\Delta_{1,max}$. As shown in the figure, both ξ_{max} and $\Delta_{1,max}$ are weak functions of R_{dep}. Note that $\Delta_{1,max}$ appears to be more sensitive to the change of R_{dep} than ξ_{max}. Physically, from Eq. (23) the grain density (i.e., the number of equiaxed particles per unit volume) in the mushy region is inversely proportional to R_{dep} cube. Under the same cooling conditions, if R_{dep} is larger, the grain density is substantially reduced, leading to a lower amount of the solid phase in the mushy region, but a higher freeze-coat thickness. The variation of ψ_s on R_{dep} is depicted in Fig. 12(b). As R_{dep} is increased from 0.001 to 0.03, there is only a slight difference between the profiles of ψ_s over this range of R_{dep}. The effect of R_λ on ξ_{max}, $\Delta_{1,max}$ and ψ_s is presented in Table 1. It is clear that ξ_{max}, $\Delta_{1,max}$, and ψ_s are insensitive to the change of R_λ. As R_λ is increased from 0.001 to 0.01, ξ_{max} and $\Delta_{1,max}$ increase only by 0.06% and 0.2%, respectively. By comparing Table 1 to Fig. 12(a), the values of ξ_{max} and $\Delta_{1,max}$ are more sensitive to the change of R_{dep} than that of R_λ.

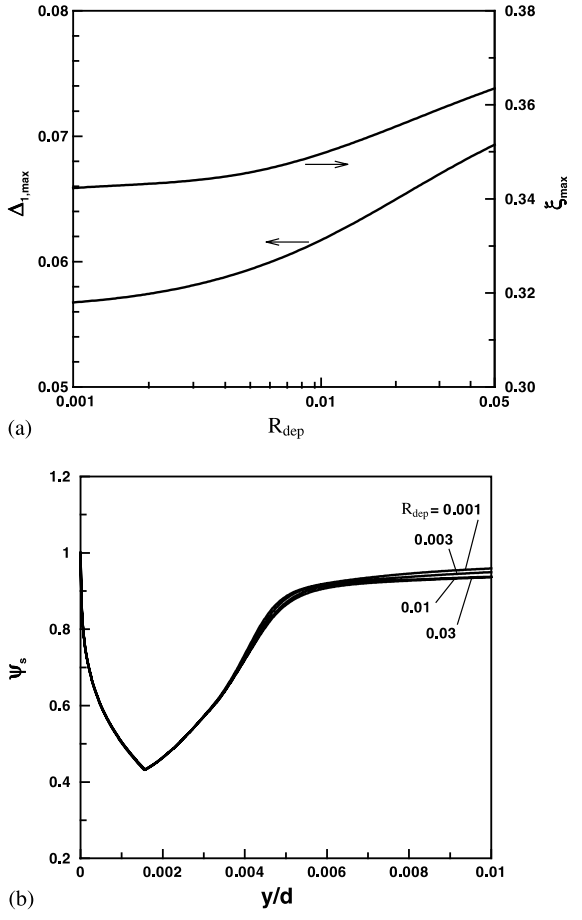

Fig. 12. Effects of the depart-diameter-to-plate-thickness ratio ($R_{sup} = 5$, $R_k = 1$, $R_{cap} = 1$, $R_{sup} = 1$, $Pr = 0.1$, $Le = 1000$, $Ste = 0.1$, $\kappa = 0.3$, $\varepsilon_{s,p} = 0.6$, and $R_\lambda = 0.005$) on (a) the maximum freeze coat thickness and the corresponding axial location and (b) the normalized species concentration of the freeze coat.

5. Conclusions

A theoretical and numerical study of the process of freeze coating of a binary substance has been performed. Based on the numerical results obtained in this study, the following conclusions can be made:

(i) The present model predicts a similar behavior for the freeze-coat thickness compared to the one reported in [11]. In general, the freeze coat grows at first, reaching a maximum, and then decays through remelting as the local wall temperature rises toward the solidus point. However, only the present model can bring about the variations of the species concentration and macrosegregation of the freeze coat.
(ii) Macrosegregation could be important in the freeze-coating process. As the distance from the surface of the plate is increased, the solid species concentration considerably decreases, reaching a minimum value and rising toward the ambient concentration. A reduction of the solid species concentration is caused by the vertical flow. In contrast, the species source term gives an opposite effect on the solid species concentration. In the early stage of solidification, the effect of the suction flow tends to dominate that of the source term.
(iii) The macrosegregation pattern is most sensitive to the equilibrium partition ratio. As the latter is increased, the difference between the solid and liquid species concentrations tends to decrease, leading to a substantial reduction of macrosegregation within the freeze coat. From an optimum-design point of view, selection of the alloy constituents or the alloy composition that maximizes the value of the equilibrium partition ratio, would lead to the best quality in the final product.
(iv) For a given set of the controlling parameters, the freeze-coat thickness predicted by the present model

is slightly larger than that reported in [11] at the same axial location because of the increasing solidus temperature due to the flow in the transverse direction, especially near the inlet.

References

[1] H.K. Kuiken, Solidification of a liquid on moving sheet, Int. J. Heat Mass Transfer 20 (4) (1977) 309–314.

[2] R.V. Seeniraj, T.K. Bose, Freeze-coating on a continuous moving sheet and an axially moving cylinder, Wärme Stoffübertragung/Thermo Fluid Dynam. 15 (4) (1981) 239–243.

[3] F.B. Cheung, Thermal boundary layer on a continuous moving plate with freezing, J. Thermophys. Heat Transfer 1 (4) (1987) 335–342.

[4] F.B. Cheung, S.W. Cha, Finite-difference analysis of growth and decay of a freeze coat on a continuous moving cylinder, Numer. Heat Transfer 12 (1) (1987) 41–56.

[5] A. Rezaian, D. Poulikakos, Heat and fluid flow process during the coating of a moving surface, J. Thermophys. Heat Transfer 5 (2) (1991) 192–198.

[6] K.G. Mahmoud, Numerical analysis of freeze coating on a two-dimensional moving plate, Numer. Heat Transfer A 25 (1994) 279–293.

[7] R. Stevens, D. Poulikakos, Freeze coating of a moving substrate with a binary alloy, Numer. Heat Transfer A 20 (4) (1991) 409–432.

[8] H. Zhang, M.K. Moallemi, Numerical simulation of hot-dip metallic coating process, Int. J. Heat Mass Transfer 38 (2) (1995) 241–257.

[9] W.D. Bennon, F.P. Incropera, A continuum model for momentum, heat and species transport in binary solid–liquid phase change system—I: model formulation, Int. J. Heat Mass Transfer 30 (10) (1987) 2161–2170.

[10] C. Tangthieng, F.B. Cheung, S.W. Shiah, Behavior of the two-phase mushy zone during freeze coating on a continuous moving plate, J. Heat Transfer 124 (1) (2002) 111–119.

[11] C. Tangthieng, F.B. Cheung, Y.C. Shih, Growth and decay characteristics of the solidified layer during freeze coating of a binary substance, J. Thermophys. Heat Transfer 16 (3) (2002) 379–388.

[12] C. Prakash, Two-phase model for binary solid–liquid phase change. Part I: governing equations, Numer. Heat Transfer B 8 (2) (1990) 131–145.

[13] J. Ni, C. Beckermann, A volume-averaged two-phase model for transport phenomena during solidification, Metall. Trans. B 22 (3) (1991) 339–361.

[14] J. Ni, F.P. Incropera, Extension of the continuum model for transport phenomena occurring during metal alloy solidification. I. the conservation equations, Int. J. Heat Mass Transfer 38 (7) (1995) 1271–1284.

[15] M.C. Schneider, C. Beckermann, A numerical study of the combined effects of microsegregation, mushy zone permeability and contraction driven flow on macrosegregation and eutectic formation in binary alloy solidification, Int. J. Heat Mass Transfer 38 (18) (1995) 3455–3473.

[16] C.Y. Wang, C. Beckermann, Equiaxed dendritic solidification with convection. Part I: multiscale/multiphase modeling, Metall. Mater. Trans. 27A (9) (1996) 2754–2764.

[17] J. Ni, F.P. Incropera, Extension of the continuum model for transport phenomena occurring during metal alloy solidification. II. Microscopic considerations, Int. J. Heat Mass Transfer 38 (7) (1995) 1285–1296.

[18] W.D. Bennon, F.P. Incropera, A continuum model for momentum, heat and species transport in binary solid–liquid phase change system—II: application to solidification change systems, Int. J. Heat Mass Transfer 30 (10) (1987) 2171–2187.

[19] C. Beckermann, R. Viskanta, Double-diffusive convection during dendritic solidification of a binary alloy, Physicochem. Hydrodynam. 10 (2) (1988) 195–213.

[20] V.R. Voller, A.D. Brent, C. Prakash, The modeling of heat, mass and solute transport in solidification systems, Int. J. Heat Mass Transfer 32 (9) (1989) 1718–1731.

[21] C.Y. Wang, C. Beckermann, Equiaxed dendritic solidification with convection. Part II: numerical simulations for an Al–4 wt pct Cu alloy, Metall. Mater. Trans. 27A (9) (1996) 2765–2783.

[22] C. Prakash, Two-phase model for binary solid–liquid phase change. Part II: some illustrative examples, Numer. Heat Transfer B 8 (2) (1990) 147–167.

[23] A.V. Kuznetsov, Investigation of the coupled heat transfer, fluid Flow and the solute transport during the strip casting process, Int. J. Heat Mass Transfer 40 (12) (1997) 2949–2961.

[24] A.V. Kuznetsov, Parametric study of macrosegregation in the horizontal strip casting process for different cooling rates and different casting speeds, Heat Mass Transfer 35 (3) (1999) 197–203.

[25] S. Fukusako, M. Yamada, Solidification of pure liquids and liquid mixtures inside ducts and over external bodies, Appl. Mech. Rev. 47 (Part 1) (1994) 590–621.

[26] F.B. Cheung, M. Epstein, Solidification and melting in fluid flow, Adv. Transport Process. 3 (1984) 35–117.

[27] S.C. Flood, L. Kategerman, V.R. Voller, The calculation of macrosegregation and heat and fluid flows in the dc casting of aluminum alloys, in: Modeling of Casting, Welding and Advanced Solidification Processes V, TMS, Warrendale, PA, 1991, pp. 683–690.

[28] C. Tangthieng, Macroscopic and microscopic modeling of freeze coating of a binary substance on a moving continuous object, Ph.D. Dissertation, The Pennsylvania State University, University Park, PA, 2002.

[29] D.R. Poirier, Permeability for flow of interdendritic liquid in columnar–dendritic alloys, Metall. Trans. B 18 (1) (1987) 245–256.

[30] H.C. de Groh III, P.D. Weidman, D. Zakhem, S. Ahuja, C. Beckermann, Calculation of dendrite settling velocities using a porous envelope, Metall. Trans. B 24B (1993) 749–753.

[31] C.Y. Wang, S. Ahuja, C. Beckermann, H.C. de Groh III, Multiparticule interfacial drag in equiaxed solidification, Metall. Trans. B 26B (1995) 111–119.

[32] S. Ahuja, C. Beckermann, R. Zakhem, P.D. Weidman, H.C. de Groh III, Drag coefficient of an equiaxed dendrite settling in an infinite medium, in: Micro/Macro Scale

Phenomena in Solidification, ASME HTD-Vol. 218/AMD-Vol. 139, New York, NY, 1992, pp. 85–91.
[33] S.V. Patankar, Numerical Heat Transfer and Fluid Flow, McGraw-Hill, New York, 1980, pp. 81–83.
[34] D.A. Anderson, J.C. Tannehill, R.H. Pletcher, Computational Fluid Mechanics and Heat Transfer, McGraw-Hill, New York, 1984, pp. 337–339.